Salt-Fingers in the Presence of Uniform Shear

Justin M. Brown[1] **and Timour Radko**[1]

[1]Naval Postgraduate School

Key Points:

- We have developed a pseudo-spectral code for investigating incompressible flows in the presence of shear
- We have found that, for typical oceanic values, current models may overpredict typical salt-fingering fluxes by at least a factor of two
- The reduction of salt finger fluxes in shear can be explained by the suppression of individual harmonics by external flows

Corresponding author: Justin M. Brown, jmbrown2@nps.edu

Abstract

Salt fingers occur throughout a large fraction of the World Ocean and can have substantial effects on large-scale mixing processes, such as the Meridional Overturning Circulation (see, e.g., Zhang et al., 1998). However, most numerical and laboratory studies of this phenomenon occur in quiescent environments. We simulate salt fingers in the presence of constant and oscillating shear in order to quantify the mixing of heat and salt by these systems under the impacts of large-scale internal waves. The code used in these simulations (the "Rocking Ocean Modeling Environment" or ROME) is a new pseudo-spectral hydrodynamic model which incorporates a steady or oscillatory background shear flow with a spatially uniform background velocity gradient. This configuration presents a challenge for modeling via Fourier-based algorithms because the typical evolution of such a flow is incompatible with the periodic boundary conditions at the vertical extremities of the computational domain. This complication is addressed by reformulating the governing equations in a new, temporally varying "tilting" coordinate system associated with the background flow as has been done in the past in the field of homogenous turbulence. Generally, it is shown that the application of shear can reduce fluxes by a factor of 2 or 3 for typical amplitudes of near-inertial waves and that the impact of shear decreases as the frequency of the applied shear increases. Though the focus of this study is on the effects of shear on double-diffusive systems, ROME is well-suited to a wide range of problems involving sheared stratified systems.

Plain Language Summary

This work seeks to understand a process known as salt fingering and investigates how this process can be affected by currents and waves in the ocean. Salt fingers occur in regions where warm and salty water exists above cooler and fresher water. This can happen in a large fraction of the ocean when the amount of evaporation exceeds the amount of precipitation and typically exists at a layer of the ocean where the temperature changes quickly with depth, known as the thermocline. These salt fingers can transport heat and salt vertically in the ocean, which can have consequences for our understanding of processes that determine large-scale features in the World Ocean. However, these salt fingers are relatively small (on the order of a few centimeters in width) and can be easily disrupted by fluid motion, such as currents and waves. We show through a series of computational experiments involving steady and oscillating motions that—for typical values in the ocean—the transport of heat and salt by these salt fingers can be easily halved.

1 Introduction

Salt fingers remain an important topic in the field of oceanography due to their omnipresence throughout mid-latitudes in the thermocline. They are also notable for their potential to form large-scale features in these regions such as staircases which can substantially affect global transport. Salt fingers were discovered by Stern (1960) and Stommel et al. (1956) first as a fluid dynamical curiosity of a "salt fountain," where the salinity could destabilize a stably stratified fluid. Though the complete theory of double diffusion took decades to develop, Stern (1960) effectively derived the condition for instability of this salt fountain, given in terms of the density ratio, R_ρ:

$$1 < R_\rho \equiv \frac{\alpha^* \frac{\partial T^*_{\text{tot}}}{\partial z^*}}{\beta^* \frac{\partial S^*_{\text{tot}}}{\partial z^*}} < \frac{\kappa^*_T}{\kappa^*_S}, \tag{1}$$

where α^* is the coefficient of thermal expansion, β^* is the coefficient of haline contraction, T^*_{tot} is the total temperature field, S^*_{tot} is the total salinity field, κ^*_T is the diffusivity of temperature, and κ^*_S is the diffusivity of salt. We use asterisks to denote dimensional quantities in order to distinguish them from their non-dimensional counterparts later. This instability takes the form of small finger-like plumes throughout the fluid and

hence became known as salt fingering or fingering convection. A full review of salt fingers is beyond the scope of this publication, but the authors recommend Radko (2013) as a comprehensive guide to double-diffusive processes. However, much of the numerical and experimental literature focuses on the behaviors of salt fingers in quiescent environments by ignoring the effects of shear and internal waves, which are present throughout the ocean.

The first systematic study of salt fingers in the presence of shear was performed in theoretical and experimental work by Linden (1974) as a follow-up to his initial publication of salt fingers in generic turbulence (Linden, 1971). He found that salt fingers are generally stabilized by the presence of turbulence or shear, and sheared fingers show the development of salt sheets, structures that look similar to salt fingers transverse to the applied shear but with long extents in the sheared direction. This is due to the ability of shear to suppress salt fingers in the direction of the shear but not transverse to it. Further lab experiments by Fernandes and Krishnamurti (2010), numerical experiments by Kimura and Smyth (2007), and observations by Kunze et al. (1987) found that the fingers themselves can tilt under the impact of shear and that the flux of salt through these systems decreases substantially as the shear increases. It was later shown by Kimura and Smyth (2011) that the equilibrium fluxes of a salt-fingering system are reached when the nonlinearities of the problem become important and a secondary instability—which they termed the "zig-zag" instability—develops between the salt sheets. This secondary instability has an analogy in the typical salt-fingering case, which was explained in Radko and Smith (2012) by the theory of growth-rate balance. This theory postulates that when the secondary instability grows at a comparable rate to the primary fingering instability that the system reaches equilibrium, and this theory has shown substantial power to predict fluxes in the case without shear.

These studies have informed our understanding of salt fingers in more complex environments, but with advances in numerical capabilities, we can investigate shear flows more in line with typical oceanic conditions. Near-inertial waves in the ocean, for example, tend to produce shear that changes direction over time. Kunze (1990) hypothesized that the horizontal banding in shadowgraph profiles east of Barbados showed the effects of such near-inertial waves. Because of the gradual change in direction, the salt fingers are suppressed isotropically. This led to the simulations of Radko et al. (2015), who sheared salt fingers in a periodic environment with gradually changing shear direction, using a sinusoidal profile for the shear instead of the hyperbolic tangent profile used by Kimura and Smyth (2007). These simulations also investigated the effects of the internal wave frequency on the finger structure and fluxes. That the fluxes are much reduced in the sheared system was confirmed, and the frequency proved only to have a moderate impact on the system. However, the simulations by Radko et al. (2015) face one major issue, which is that the domain size (typically 1–2m) limits the vertical scale of the modeled internal waves, which are typically on very large scales.

We address this limitation by introducing a model which enforces shear globally throughout the simulation, effectively permitting an infinite internal wave wavelength. We introduce a new numerical model, which we call our Rocking Ocean Modeling Environment (ROME). This model uses a pseudo-spectral method to evolve the incompressible fluid equations in a "rocking" system that can include the effects of oscillating or constant shear. Though this study focuses on the impact of shear on a double-diffusive system, ROME is far more generally applicable to micro-scale studies of the effects of shear on stratified systems. We simulate a salt fingering unstable fluid under the impact of constant and oscillating shear using similar parameters to the Radko et al. (2015) study. These were decided in order to most directly compare the effects of finite wavelength shear with infinite wavelength shear. We find that the previous study substantially underestimates the effects of the angular frequency on the fluxes of these systems, which can completely damp fingering convection at low (near-inertial) frequencies and only moderately

reduce the fluxes at moderate (four times inertial) frequencies. We compare to a linear stability analysis and show that the permitted modes in cases with shear are topologically distinct in wavenumber space and that this has inherent consequences in the final fluxes of these systems.

We present our model in Section 2 and outline our simulation setup in Section 3. We discuss the fluxes of these simulations and the finger morphology in Section 4. We present the linear stability analysis in Section 5 and conclude with some final discussion in Section 6.

2 Code

2.1 Boussinesq Equations with Shear

We begin with the dimensional Boussinesq equations (see, for example, Baines & Gill, 1969):

$$\frac{\partial}{\partial t^*}\mathbf{u}^* + \mathbf{u}^*\cdot\nabla^*\mathbf{u}^* = -\frac{\nabla^* p^*}{\rho_0^*} + g^*\left(\alpha^* T^* - \beta^* S^*\right)\mathbf{e}_z + \nu^*\nabla^{*2}\mathbf{u}^* + \mathbf{F}^* \tag{2}$$

$$\frac{\partial}{\partial t^*}T^* + \mathbf{u}^*\cdot\nabla^* T^* = -w^*\frac{\partial \overline{T}^*}{\partial z^*} + \kappa_T^*\nabla^{*2}T^* \tag{3}$$

$$\frac{\partial}{\partial t^*}S^* + \mathbf{u}^*\cdot\nabla^* S^* = -w^*\frac{\partial \overline{S}^*}{\partial z^*} + \kappa_S^*\nabla^{*2}S^* \tag{4}$$

$$\nabla^*\cdot\mathbf{u}^* = 0, \tag{5}$$

where $\mathbf{u}^*$ is the total fluid velocity, p^* is the pressure perturbation away from the hydrostatic pressure, T^* is the fluid temperature perturbation away from a background field $\overline{T}^*$, S^* is the salinity concentration perturbation away from an analogous $\overline{S}^*$, and $\mathbf{F}^*$ is an arbitrary forcing function. The symbol ρ_0^* denotes a reference density, g^* is the gravitational acceleration, and ν^* is the kinematic viscosity. The vector $\mathbf{e}_z$ is the unit vector antiparallel to gravity. The background gradients $\frac{\partial \overline{T}^*}{\partial z^*}$ and $\frac{\partial \overline{S}^*}{\partial z^*}$ are assumed constant, but the actual horizontally-averaged T–S profiles are allowed to evolve in time.

Using the standard non-dimensionalization from Radko (2013), the above equations reduce to the following non-dimensional forms:

$$\frac{1}{\mathrm{Pr}}\left(\frac{\partial}{\partial t}\mathbf{u} + \mathbf{u}\cdot\nabla\mathbf{u}\right) = -\nabla p + (T - S)\,\mathbf{e}_z + \nabla^2\mathbf{u} + \mathbf{F} \tag{6}$$

$$\frac{\partial}{\partial t}T + \mathbf{u}\cdot\nabla T + sw = \nabla^2 T \tag{7}$$

$$\frac{\partial}{\partial t}S + \mathbf{u}\cdot\nabla S + sR_0^{-1}w = \tau\nabla^2 S \tag{8}$$

$$\nabla\cdot\mathbf{u} = 0, \tag{9}$$

where we have defined $s \equiv \mathrm{sign}(\frac{\partial \overline{T}^*}{\partial z^*})$; $\mathrm{Pr} \equiv \nu^*/\kappa_T^*$, the Prandtl number; $\tau \equiv \kappa_S^*/\kappa_T^*$, the inverse Lewis number; and $R_0 \equiv \alpha^*\frac{\partial \overline{T}^*}{\partial z^*}/\beta^*\frac{\partial \overline{S}^*}{\partial z^*}$, the background density ratio, and where the non-dimensional units are given by

$$[L] \equiv \left(\frac{\alpha^* g^*\left|\frac{\partial \overline{T}^*}{\partial z^*}\right|}{\nu^*\kappa_T^*}\right)^{-\frac{1}{4}}, \tag{10}$$

$$[t] \equiv \frac{[L]^2}{\kappa_T^*}, \tag{11}$$

$$[T] \equiv \left|\frac{\partial \overline{T}^*}{\partial z^*}\right|[L], \tag{12}$$

$$[S] \equiv \frac{\alpha^*}{\beta^*}[T]. \tag{13}$$

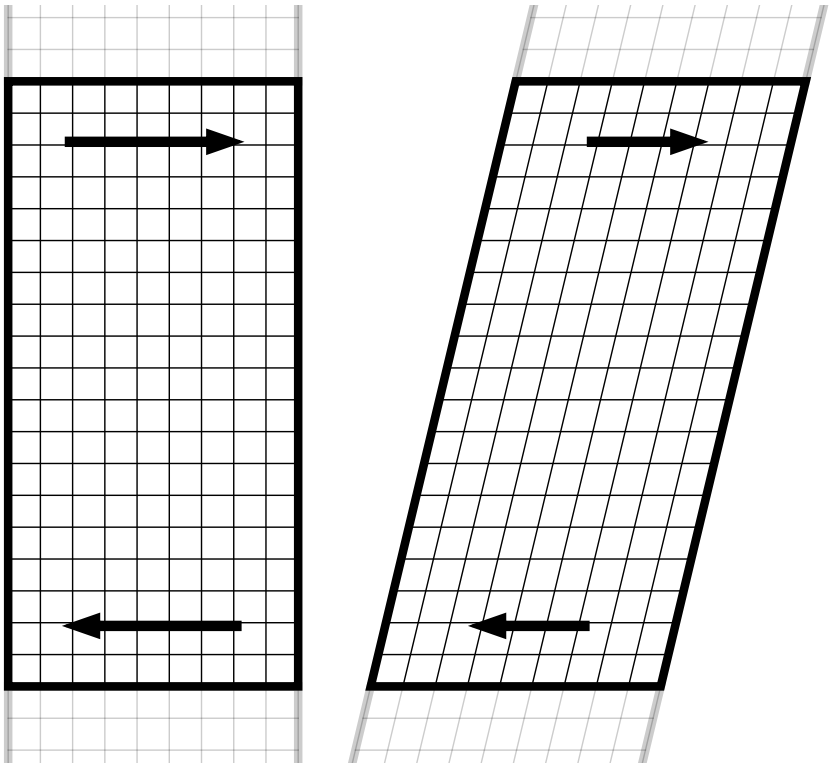

Figure 1. A basic diagram depicting the nature of the sheared coordinate system. The left figure is the starting, vertically oriented state. The arrows indicate the background velocity. As the simulation progresses, the grid evolves according to the background velocity as indicated in the right panel. The periodicity of the simulation is enforced in this sheared coordinate system.

We are interested in the application of a sheared flow with shear rate of the form $\gamma \cos \omega t$, so we separate the velocity into the velocity relative to the sheared coordinate system (denoted with a tilde) and the velocity of the coordinate system itself (denoted with an overbar): $\mathbf{u} \equiv \tilde{\mathbf{u}} + \overline{u}(z,t)\,\mathbf{e}_x + \overline{v}(z,t)\,\mathbf{e}_y$, where $\overline{u}(z,t) = \gamma_x z \cos \omega t$ and $\overline{v}(z,t) = \gamma_y z \cos(\omega t + \phi)$. Here, the quantity ϕ is the phase difference between the shears in x and y, which is typically $\pi/2$ for slow, near-inertial waves. Thus, to enforce this flow, we require that $\mathbf{F} = \frac{1}{\mathrm{Pr}} \frac{\partial}{\partial t} (\gamma_x z \cos \omega t \mathbf{e}_x + \gamma_y z \cos(\omega t + \phi) \mathbf{e}_y)$. Note that $\tilde{\mathbf{u}} = (\tilde{u}, \tilde{v}, w)$ as there is no background term for w. The unit vectors $\mathbf{e}_x$, $\mathbf{e}_y$, and $\mathbf{e}_z$ are always defined in terms of the vertically oriented (stationary) coordinates x, y, and z.

To simplify these equations, we construct a Fourier solution in the *sheared* (tilting) coordinate system, which follows the fluid displacement by the background flow. A diagram of this setup is presented in Figure 1. We introduce a change of coordinates according to

$$\tilde{x} = x - \frac{\gamma_x z}{\omega} \sin \omega t \tag{14}$$

$$\tilde{y} = y - \frac{\gamma_y z}{\omega} \sin(\omega t + \phi) \tag{15}$$

$$\tilde{z} = z \tag{16}$$

$$\tilde{t} = t. \tag{17}$$

Note that in the limit as $\omega \to 0$, $\frac{\sin(\omega t)}{\omega} \to t$, which formally recovers the case of constant shear. Numerically, this is treated as a special case (by replacing all instances of

$\frac{\sin(\omega t)}{\omega}$ with t) to avoid the singularity that arises. The system is then decomposed into Fourier modes as follows:

$$q(\mathbf{x},t) = \sum_{l=-N_x}^{N_x} \sum_{m=-N_y}^{N_y} \sum_{n=-N_z}^{N_z} q_{l,m,n}(t)\, e^{i\tilde{\mathbf{k}}_{l,m,n}\cdot\tilde{\mathbf{x}}}, \tag{18}$$

where q represents a generic field, $\tilde{\mathbf{x}} \equiv (\tilde{x},\tilde{y},\tilde{z})$, and $\tilde{\mathbf{k}}_{l,m,n} \equiv \left(l\tilde{k}_x, m\tilde{k}_y, n\tilde{k}_z\right)$. The quantities $\tilde{k}_x$, $\tilde{k}_y$, and $\tilde{k}_z$ are the lowest non-zero wave numbers in the system, which has dimensions Γ_x by Γ_y by Γ_z. This is a straightforward extension of the transformation described in Rogallo (1981) to a flow with temperature and salinity. The transformation to the $\tilde{\mathbf{x}}$ coordinate system removes the coefficients that contain $\overline{\mathbf{u}}$ and leaves only $\frac{\partial\overline{\mathbf{u}}}{\partial z}$, which has no dependence on the vertical coordinate. This leaves the only non-linear terms as the advection terms, which can be calculated in physical space, and the aliasing is removed with a 3/2-dealiasing scheme by increasing the number of Fourier modes in Equation 18 and setting those to be zero after the calculation of the non-linear terms. The full details of this transformation, the non-linear calculation, and the mode-evolution equations are included in Appendix A. The equations are integrated in time using a third-order Adams–Bashforth scheme for all but the diffusive terms and a Backwards Differentiation Formula for the implicit diffusion terms. A Patterson–Orszag method is used to enforce incompressibility, which is outlined in detail in Appendix B. Because this scheme requires knowledge of the previous timesteps, the first three steps are computed using a second-order Runge–Kutte scheme instead.

Our implementation of this algorithm uses the fast Fourier transform library FFTW3 (Frigo, 1999) and a decomposition scheme as outlined in Stellmach and Hansen (2008). The multi-processing decomposition entails splitting the domain into a number of "pencil beam" structures, which run the full length of Fourier space in the $\tilde{z}$-direction but are tiled in $\tilde{x}$ and $\tilde{y}$. It is plain from Equations A13–A17 that the linear tendency of each mode only depends on the amplitudes of $\tilde{\mathbf{u}}$, S, and T of that singular mode. Thus, no communication is needed for these terms and evaluating them with spectral accuracy is trivial. For the nonlinear terms, as explained in Appendix A, a Fourier transform is required. The transform in the $\tilde{z}$-direction is trivial on each process as the full $\tilde{z}$-column is present for each l,m mode. To perform the other two transforms, the data are transposed across the processes, as is described in Stellmach and Hansen (2008), to establish these pencil beams running instead in the $\tilde{y}$-direction, after which it is possible to perform the Fourier transform along that dimension. One more transpose and uni-directional transform complete the full three-dimensional transform. Then, the products required are purely local as they are described in Appendix A and so do not require any communication. The final products are transformed back using the aforementioned algorithm in reverse.

2.2 Remap

Perhaps the most important implication of the transform described in Equations 14–17 is that the inclination of the computational grid with respect to the vertical direction, $\frac{\partial\tilde{x}}{\partial z}$ and $\frac{\partial\tilde{y}}{\partial z}$, can become arbitrarily large, depending on the values of γ_x, γ_y, and ω. We introduce a remapping step, which serves to ensure that $\frac{\partial\tilde{x}}{\partial z}$ and $\frac{\partial\tilde{y}}{\partial z}$ are minimal at every time by transforming the coordinates to a less inclined orientation that remains periodic in $\tilde{x}$, $\tilde{y}$, and $\tilde{z}$. This is demonstrated visually in Figure 2. This problem was recognized by Rogallo (1981), and he introduced a remapping step when the computational domain became substantially deformed, though this remapping must be done with care in order to avoid aliasing errors.

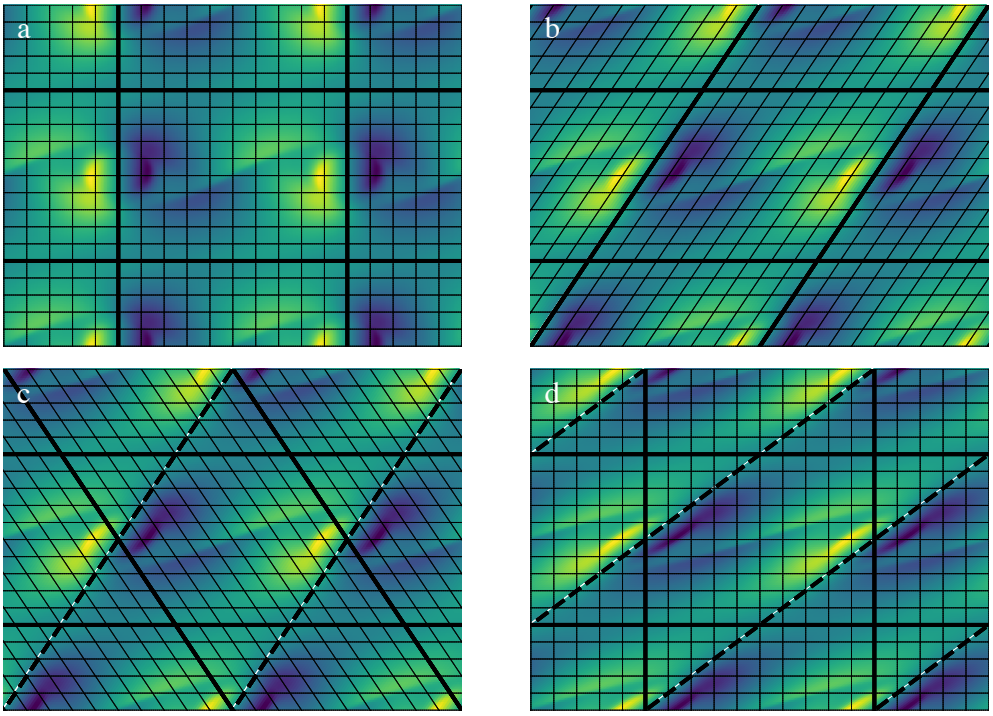

Figure 2. A time-lapse of an example simulation. The center box represents the (periodic) domain of a two-dimensional simulation. The simulation begins vertically oriented, as shown in subfigure a. As the simulation evolves, the grid progressively inclines until state b, where the system inclination is $\frac{\partial \tilde{x}}{\partial z} = \frac{\Gamma_x}{2\Gamma_z}$. At every timestep, the simulation is also periodic along inclinations $\frac{\partial \tilde{x}}{\partial z} \pm \frac{\Gamma_x}{\Gamma_z}$, so in state c, we are able to remap to a system where $\frac{\partial \tilde{x}}{\partial z} = -\frac{\Gamma_x}{2\Gamma_z}$ The dashed lines in state c show the original extent of the domain. The simulation continues to shear and reaches state d.

Canuto et al. (2007) describes how to transform from one coordinate system, $\tilde{\mathbf{x}}$, to another coordinate system of arbitrary inclination, given by

$$\tilde{x}' = \tilde{x} + a\,(\tilde{z} - \tilde{z}_0)\,, \tag{19}$$

$$\tilde{y}' = \tilde{y}, \tag{20}$$

$$\tilde{z}' = \tilde{z}, \tag{21}$$

where a is the constant difference in inclination between the two coordinate systems and $\tilde{z}_0$ is a reference point in $\tilde{z}$. Rogallo (1981) recognized that this transformation could only be performed and maintain periodicity for $a = \pm\frac{\Gamma_x}{\Gamma_z}$ or some integer multiple thereof. To minimize the inclination of the simulation, we remap when $\left|\frac{\partial\tilde{x}}{\partial\tilde{z}}\right| > \frac{\Gamma_x}{2\Gamma_z}$. This transform increases or decreases the inclination by $\frac{\tilde{k}_z}{\tilde{k}_x}$, which is equivalent to shifting the $\tilde{z} = \Gamma_z$ level forward or backward in $\tilde{x}$ by Γ_x with respect to the $\tilde{z} = 0$ level. Although this discussion was restricted to transformation in $\tilde{x}$, a similar argument holds for transforms in $\tilde{y}$. In either case, the coordinate change is performed with a Fourier transform only in $\tilde{z}$ followed by multiplying each field by $e^{\pm i l\tilde{k}_x \frac{\Gamma_x}{\Gamma_z}(z-z_0)}$, where the sign is positive if we're increasing the inclination and negative otherwise. An inverse Fourier transform completes the change of coordinates. Because the remapping scheme inherently changes the geometry of the system, some additional allowances are made for the time-integration step. As with the initial system, a second-order Runge–Kutte scheme is used for the first three steps after a remapping is completed. Once sufficient previous steps have been recorded, the simulation returns to the combined Adams–Bashforth scheme and Backwards Differentiation Formula.

However, Delorme (1985) recognized that this method for changing coordinates has the potential to introduce aliasing errors during the remap and proposed a solution to address this. Canuto et al. (2007) demonstrated this point very clearly in their Figure 3.3, and so only a truncated discussion is included here. They showed that modes with $|l\tilde{k}_x + an\tilde{k}_z| > N_z$ will be aliased. We adopt the suggestion of Delorme (1985) and set those modes that would be aliased to zero before and after the remap step. This does result in a loss of information in some of the highest-order modes and thus, resolution tests for any individual applications of this algorithm are of critical importance to ensure that associated error does not substantially affect the results.

3 Simulations

Each simulation has physical extent of $\Gamma_x = \Gamma_y = 50$ and $\Gamma_z = 100$ and is resolved by 128 Fourier modes in each horizontal dimension and 256 Fourier modes in the vertical. The system has a density ratio of $R_0 = 2$, a diffusivity ratio of $\tau = 0.01$, and a Prandtl number of $\mathrm{Pr} = 10$. The simulations were seeded with small perturbations taken from a uniform random distribution in T and S but otherwise began with uniform temperature, salinity, and velocity perturbations. The shear magnitudes, γ_x and γ_y, and the frequency of the shear are varied between the simulations. The simulations are of three primary shear regimes: constant shear, unidirectional oscillating shear, and rotating shear. In the constant and unidirectional oscillating shear cases, the y-component of the shear is set to $\gamma_y = 0$, and in the rotating shear case, $\gamma_y = \gamma_x$ and $\phi = \pi/2$. The simulation parameters are tabulated in Table 1, and the analogous mean Richardson numbers are also tabulated for convenience, which take the form of

$$\mathrm{Ri} = \frac{\mathrm{Pr}\,(R_0 - 1))}{\gamma_x^2} \tag{22}$$

for the constant and rotating shear cases in our non-dimensional system and

$$\mathrm{Ri} = 2\frac{\mathrm{Pr}\,(R_0 - 1))}{\gamma_x^2} \tag{23}$$

Table 1. Simulation Parameters

Case	Ri	γ_x	γ_y	ω
1	∞	0	0	0
2	8	$\sqrt{5/8}$	0	0
3	4	$\sqrt{5/4}$	0	0
4	2	$\sqrt{5/2}$	0	0
5	4	$\sqrt{5/2}$	0	0.1π
6	4	$\sqrt{5/2}$	0	0.2π
7	4	$\sqrt{5/2}$	0	0.3π
8	4	$\sqrt{5/2}$	0	0.4π
9	8	$\sqrt{5/8}$	$\sqrt{5/8}$	0.1π
10	8	$\sqrt{5/8}$	$\sqrt{5/8}$	0.2π
11	8	$\sqrt{5/8}$	$\sqrt{5/8}$	0.3π
12	8	$\sqrt{5/8}$	$\sqrt{5/8}$	0.4π
13	4	$\sqrt{5/4}$	$\sqrt{5/4}$	0.1π
14	4	$\sqrt{5/4}$	$\sqrt{5/4}$	0.2π
15	4	$\sqrt{5/4}$	$\sqrt{5/4}$	0.3π
16	4	$\sqrt{5/4}$	$\sqrt{5/4}$	0.4π
17	2	$\sqrt{5/2}$	$\sqrt{5/2}$	0.1π
18	2	$\sqrt{5/2}$	$\sqrt{5/2}$	0.2π
19	2	$\sqrt{5/2}$	$\sqrt{5/2}$	0.3π
20	2	$\sqrt{5/2}$	$\sqrt{5/2}$	0.4π

for the case of oscillating unidirectional shear, where the additional factor of two accounts for the temporal average of the oscillations in γ_x^2 being half of the maximum.

In each simulation, the primary quantities of interest are the vertical thermal and haline fluxes, which are measured respectively as

$$F_T = -\langle wT \rangle, \tag{24}$$

$$F_S = -\langle wS \rangle, \tag{25}$$

where the angled brackets indicate the spatial average of the quantity in the domain. These quantities are related through our non-dimensionalization to the Nusselt numbers by $\mathrm{Nu}_T - 1 = F_T$ and $\mathrm{Nu}_S - 1 = R_0 F_S/\tau$. We continue each simulation until the system achieves a quasi-steady equilibrium in these fluxes and then continue the simulation until it remains at this equilibrium for at least 100 time units. For statistical purposes, we estimate the final state of the thermal and haline fluxes in these simulations as the time average over the final 100 time units, which we represent as $\overline{F}_T$ and $\overline{F}_S$, respectively.

4 Results

We plot the time evolution of the thermal and haline fluxes for several unidirectional simulations in Figure 3. Most of these have $\mathrm{Ri} = 4$; however, we also include the case without shear as a point of comparison. In the early stages of the simulations, the perturbations are weak, and the nonlinear terms are therefore vanishingly small. In this regime, the system is well approximated by only its linear terms, the solution to which is an exponential. This exponential growth is apparent in the earliest stages of the simulations (i.e., prior to $t = 80$). After the nonlinear terms become important, the fluxes eventually equilibrate as the system achieves a quasi-steady balance. The level of this

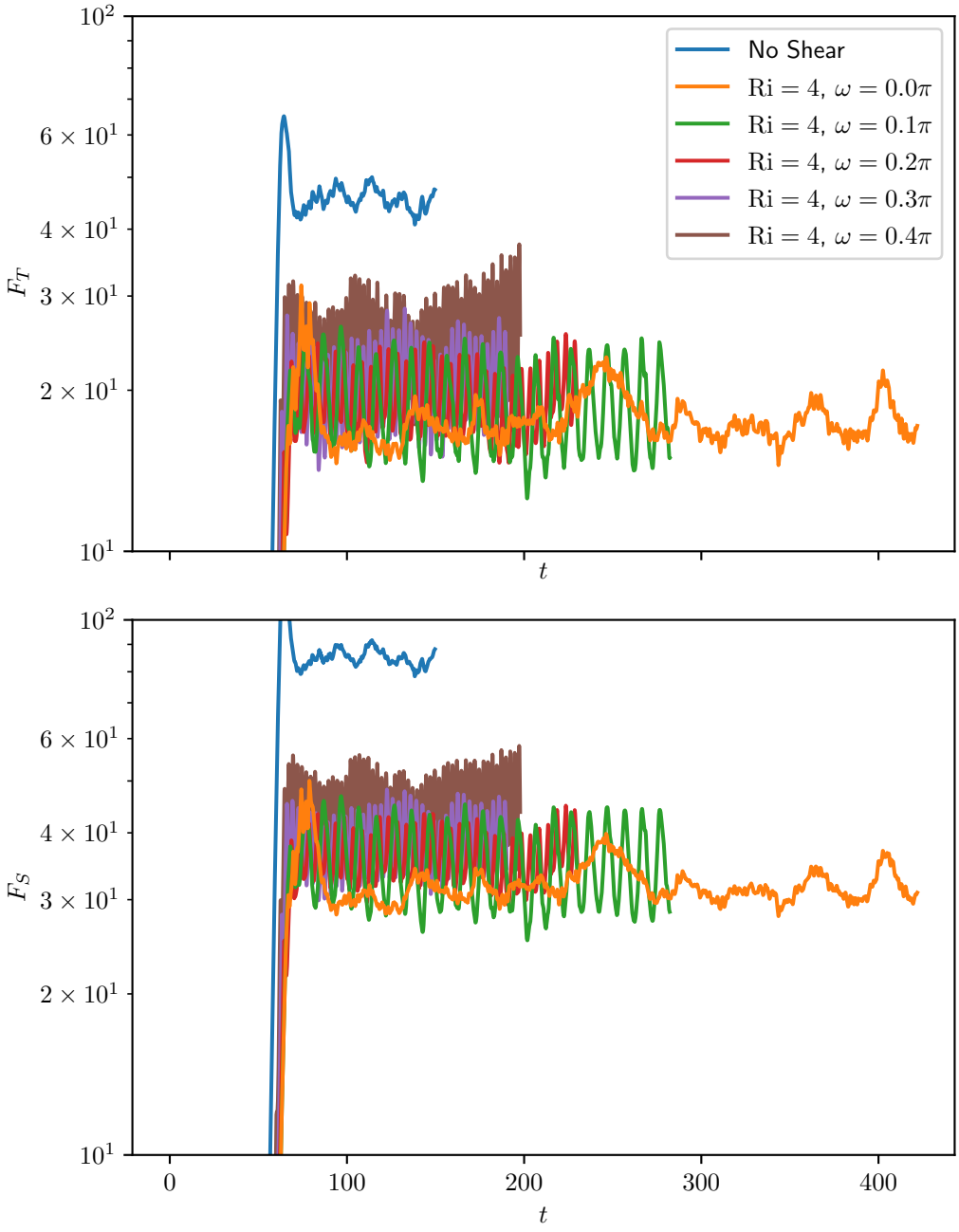

Figure 3. (top) The time evolution of the spatially averaged thermal fluxes from oscillatory simulations with mean Ri=4 (including the case with constantly directed shear for comparison). (bottom) The haline fluxes for the same simulations.

equilibration is taken to represent the typical fluxes of these systems. All sheared simulations presented in Figure 3 show reduced fluxes—both thermal and haline—from the base case without shear by more than a factor of 2. This effect is due, as will be shown in Section 5, to shear's capacity to damp the fingering instability. This damping, however, is not reflected in the exponential growth rate of the early linear system, but the lower fluxes in the linear stage do correlate to lower fluxes upon saturation. There is a weak correlation of both thermal and haline fluxes with ω, with higher frequencies having larger fluxes. We attribute this effect to the higher frequencies (for the same γ_x) resulting in less deformation of the system and therefore less inhibition of the salt-fingering modes. We present a rendering of the unidirectionally oscillating simulation with $\mathrm{Ri} = 4$ and $\omega = 0.1\pi$ in Figure 4. This figure shows the salinity perturbation of the simulation, and the main visible features are the finger structures apparent in the y–z plane. These fingers are strongly distorted in the x direction by the application of shear. This asymmetry is present only in the unidirectional shear cases and is consistent with other studies that have shown the development of laterally uniform sheets in sheared salt-fingering problems, as in Kimura and Smyth (2011).

Figure 5 shows the same time series of the fluxes for the simulations with a rotating shear profile and with $\mathrm{Ri} = 2$. These simulations show the most dramatic disparity from the simulations with sinusoidal shear profiles presented in Radko et al. (2015). The general trend is the same as in the cases presented in Figure 3, where higher frequencies have larger fluxes; however, the difference in fluxes is much more substantial in these cases. The case with the lowest frequency, $\omega = 0.1\pi$, develops with substantially lower fluxes than all other cases in this study, almost two orders of magnitude lower than the case with the same Richardson number but constant shear. This illustrates an important distinction between the unidirectional oscillating shear flow and the rotating case, where the rotation of the shear profile effectively removes any preference of the system for direction. This is visually apparent in Figure 6, which shows the salinity perturbation for the rotating case with $\mathrm{Ri} = 2$ and $\omega = 0.1\pi$. This simulation shows no predilection to the development of any form of salt sheets as all modes are effectively inhibited by shear in the system. This will be shown in depth through an analysis of linear theory in Section 5.

We summarize our simulations in Figure 7, which shows the time averages of the thermal and haline fluxes, as described in Section 3. The case without shear is presented as a cross, and it exceeds all of the sheared simulations by a wide margin regardless of the choices of shear direction, magnitude, or frequency, which is consistent with the understanding that shear generally serves to inhibit the salt-fingering instability. This is also consistent with the trend in Richardson number, which shows that simulations with weaker shear (i.e., higher Richardson number) demonstrate larger fluxes almost universally regardless of the choice of shear profile. In addition, there is a strong dependence of the fluxes on ω, again showing the aforementioned trend observed both in Figures 3 and 5. On this front, we see one of the first major deviations from the results of Radko et al. (2015), who used a sinusoidal shear profile and whose simulations are also plotted in Figure 7. His simulations showed that the case of unidirectional shear demonstrated an inverse dependence of fluxes on ω. This may be due to the oscillations in that case taking the form of standing waves instead of traveling waves, which would have been more comparable to the effects of passing internal waves and more consistent with the setup used in this study. Our case of unidirectional shear shows larger fluxes than the cases with the same Richardson number but with rotating shear, and this is consistent with the concept that unidirectional shear only inhibits salt-fingering modes in the plane of the shear itself.

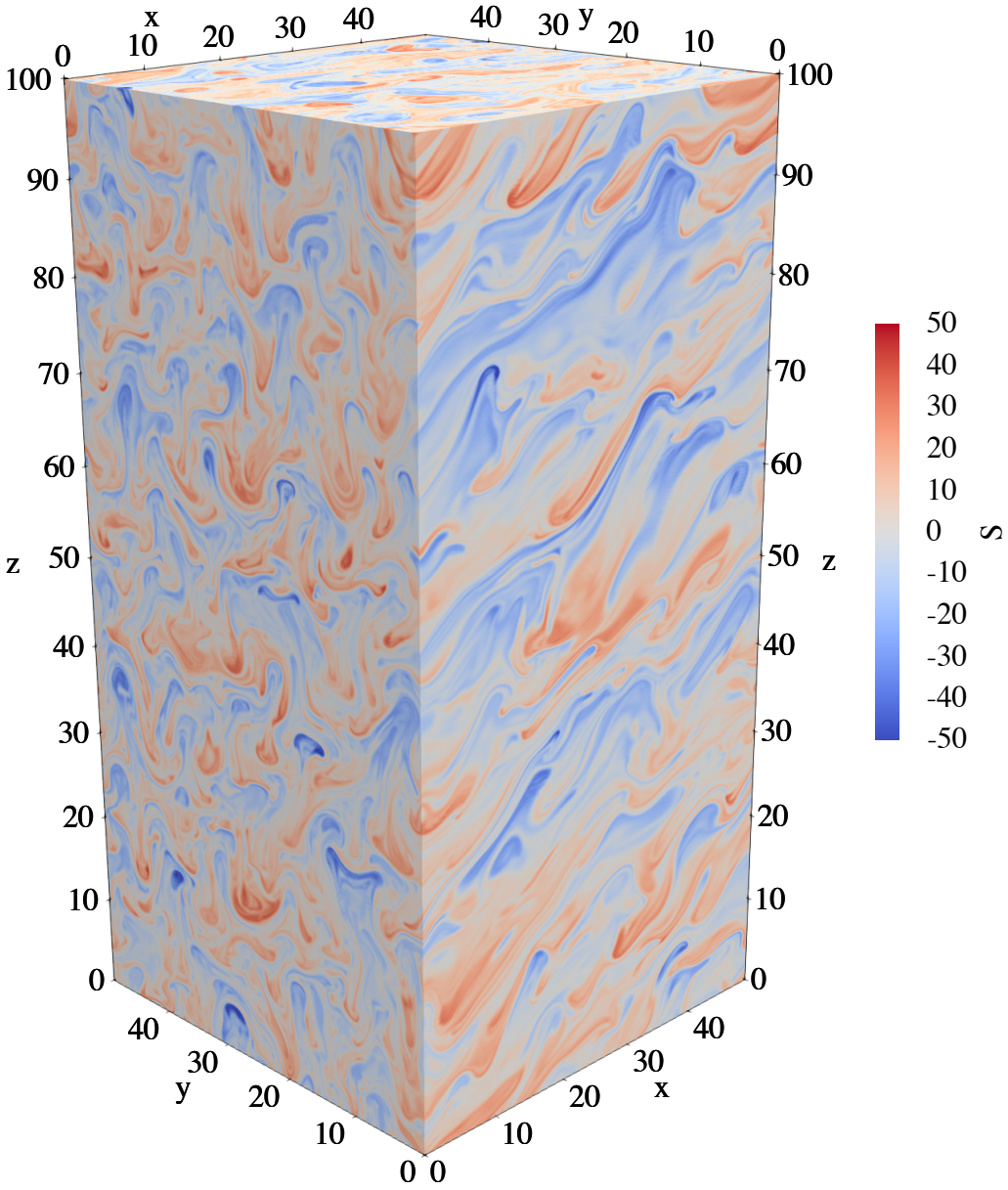

Figure 4. (top) The salinity perturbation field for a unidirectional oscillating shear simulation with Ri = 4 and $\omega = 0.1\pi$.

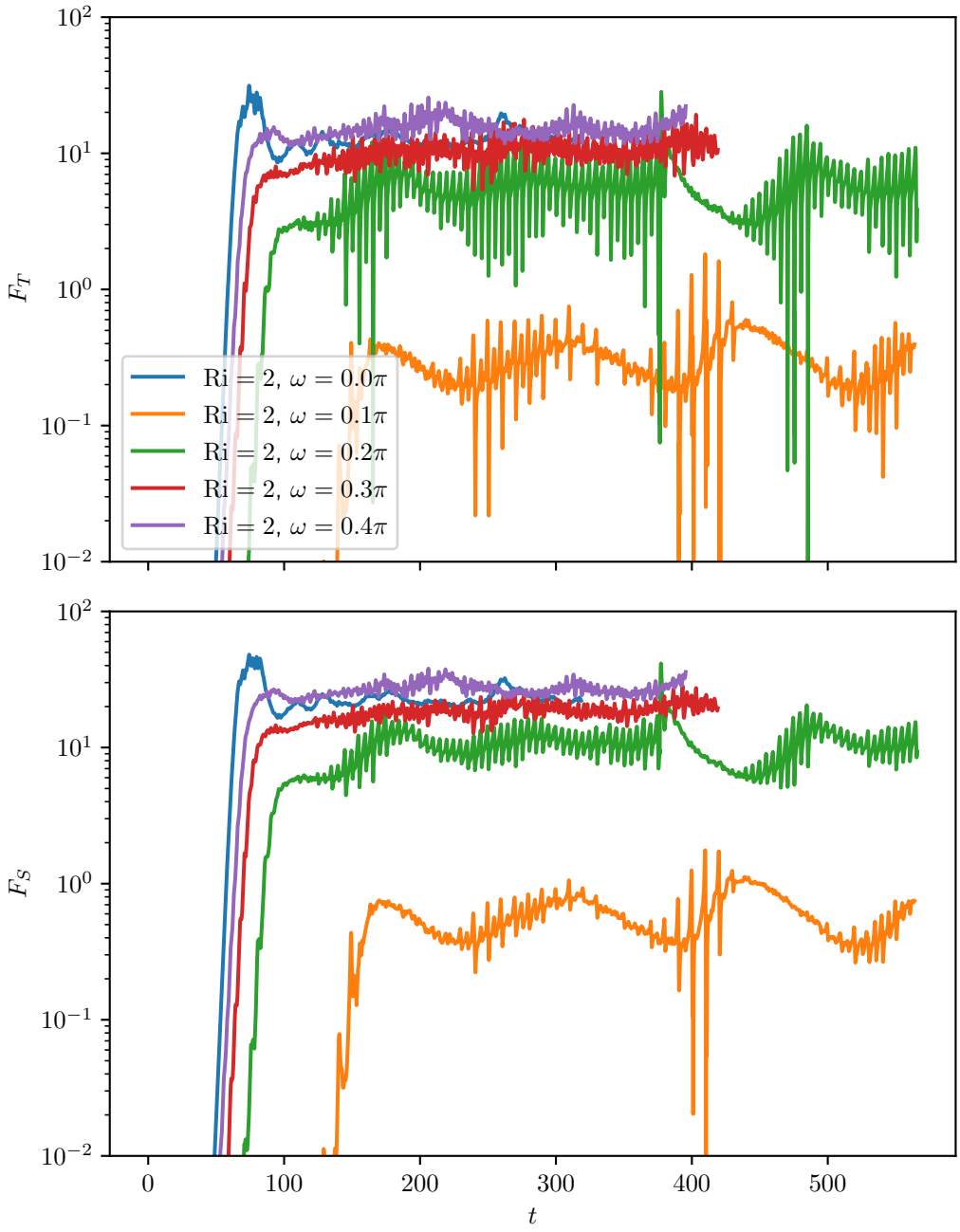

Figure 5. (top) The time evolution of the spatially averaged thermal fluxes from rotating simulations with Ri=2 (including the case with constantly directed shear for comparison). (bottom) The haline fluxes for the same simulations.

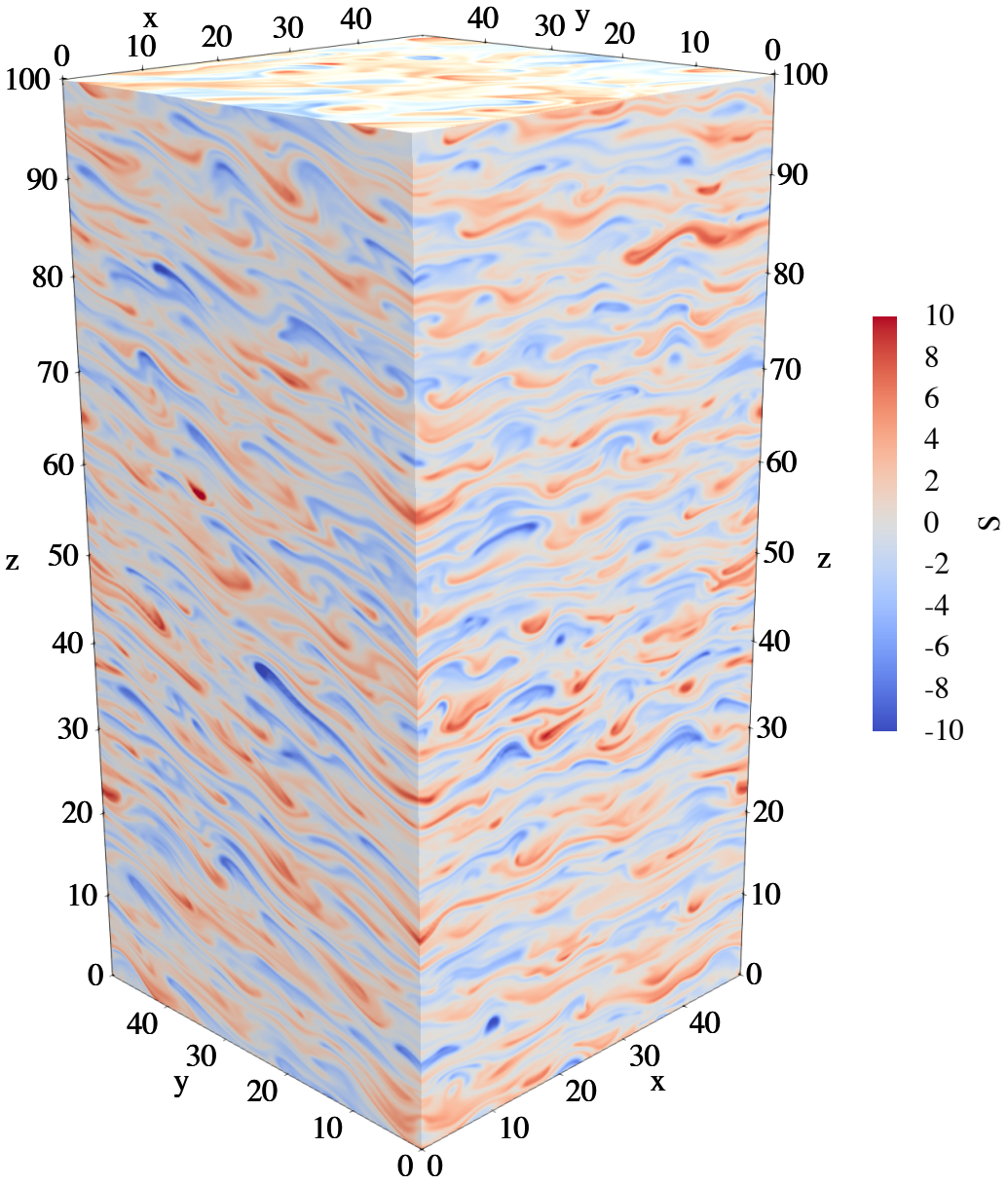

Figure 6. (top) The salinity perturbation field for a rotating shear simulation with Ri = 2 and $\omega = 0.1\pi$.

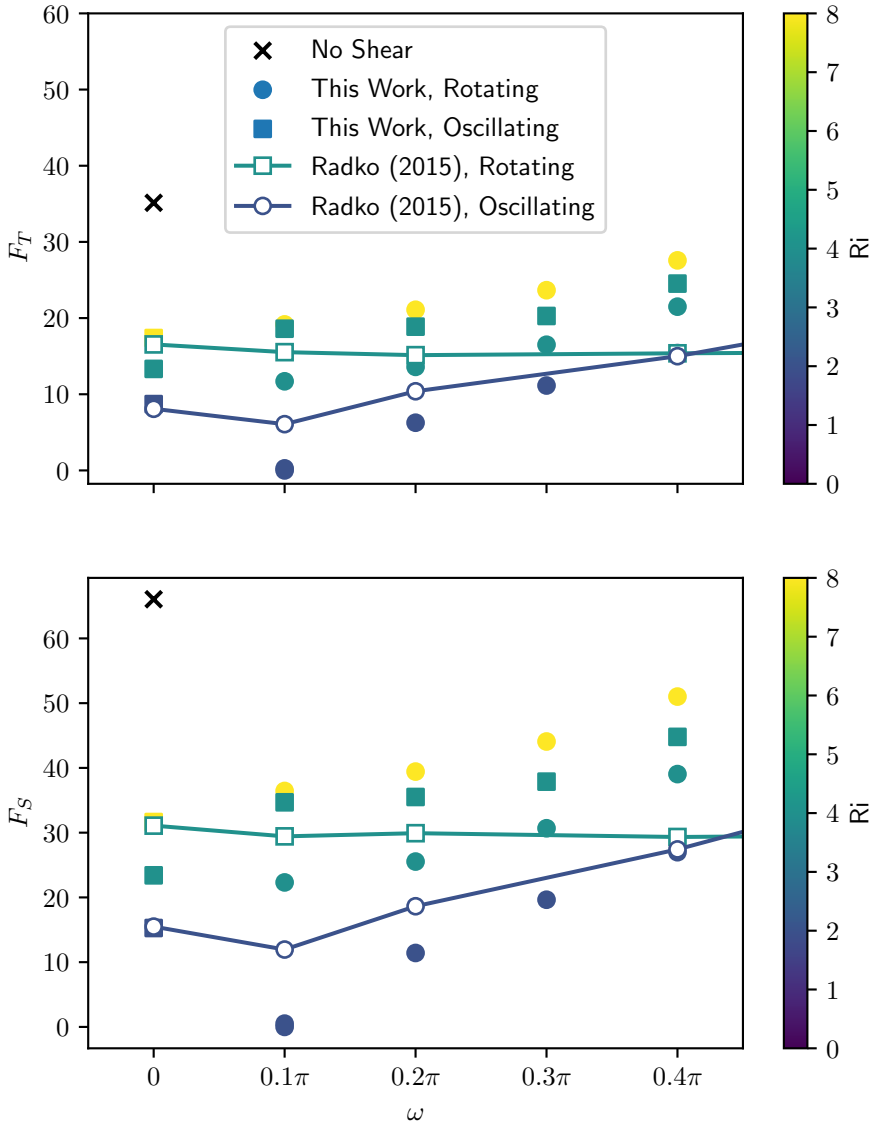

Figure 7. (top) The temporal and spatial averages of the thermal fluxes from all simulations as a function of the angular frequency of shear, colored in accordance with mean Richardson number. (bottom) The averaged haline fluxes for all simulations.

5 Linear Theory

In order to understand the dependence of the fluxes on the shear profile, we turn to linear stability. We construct the linear forms of Equations A13–A17 in terms of the perturbed fields, $\tilde{\mathbf{u}}$, S, T, and p and assume single-mode solutions of the form $q = Q(t)e^{i\tilde{\mathbf{k}}_\mathrm{M}\cdot\tilde{\mathbf{x}}}$, where Θ and Σ denote the time-dependent amplitude for T and S, respectively. These equations are given by

$$\frac{1}{\mathrm{Pr}}\left(\frac{\partial}{\partial\tilde{t}}\tilde{U} + W\frac{\partial\overline{u}}{\partial z}\right) = -i\tilde{k}_{\mathrm{M},x}P - \mathbf{k}_\mathrm{M}^2\tilde{U}, \tag{26}$$

$$\frac{1}{\mathrm{Pr}}\left(\frac{\partial}{\partial\tilde{t}}\tilde{V} + W\frac{\partial\overline{v}}{\partial z}\right) = -i\tilde{k}_{\mathrm{M},y}P - {\mathbf{k}_\mathrm{M}}^2\tilde{V}_{l,m,n}, \tag{27}$$

$$\frac{1}{\mathrm{Pr}}\frac{\partial}{\partial\tilde{t}}W = -ik'_\mathrm{M}P - {\mathbf{k}_\mathrm{M}}^2W + \Theta - \Sigma, \tag{28}$$

$$\frac{\partial}{\partial\tilde{t}}\Theta + sW = -\mathbf{k}_\mathrm{M}^2\Theta, \tag{29}$$

$$\frac{\partial}{\partial\tilde{t}}\Sigma + sR_0^{-1}W = -\tau\mathbf{k}_\mathrm{M}^2\Sigma, \tag{30}$$

$$\tilde{k}_{\mathrm{M},x}\tilde{U} + \tilde{k}_{\mathrm{M},y}\tilde{V} + k'_\mathrm{M}W = 0, \tag{31}$$

where $\mathbf{k}_\mathrm{M}^2 \equiv \tilde{k}_{\mathrm{M},x}^2 + \tilde{k}_{\mathrm{M},y}^2 + {k'_\mathrm{M}}^2$ and $k'_\mathrm{M} \equiv \tilde{k}_{\mathrm{M},z} - \tilde{k}_{\mathrm{M},x}\frac{\gamma_x}{\omega}\sin\omega\tilde{t} - \tilde{k}_{\mathrm{M},y}\frac{\gamma_y}{\omega}\sin(\omega\tilde{t}+\phi)$. We numerically evolve all the mode amplitudes from small initial values using a variable-order backwards difference formula out to $t = 100$ and estimate the growth rate of the mode by fitting the temporal evolution to an exponential of the form $Qe^{\lambda t}$.

Figure 8 illustrates the growth rate throughout $\tilde{\mathbf{k}}_\mathrm{M}$ space for two sets of fundamental parameters: one without shear and one with constant shear. The parameters are identical to those of cases 1 and 3 on Table 1. The case without shear shows growth rates that are azimuthally symmetric in horizontal wavenumber, which simply illustrates that the basic salt-fingering instability does not show preference in horizontal directions and tends to favor horizontal wavelengths of 2π (or about 6cm for oceanic values). In addition, the strongest modes occur for $\tilde{k}_{\mathrm{M},z} = 0$, which are the vertically oriented "elevator modes" typically associated with the initial development of salt fingers; all of this is consistent with canonical understanding of the phenomenon (Radko, 2013). However, the addition of constant shear in the x direction affects some of these modes. All modes with $\tilde{k}_{\mathrm{M},x} \neq 0$ in such a case are strongly inhibited by the shear, which explains the development of the salt sheets in the typical sheared salt-fingering case, as seen in Kimura and Smyth (2007). This observation is not new but does provide useful context for our discussion. Modes with $\tilde{k}_{\mathrm{M},x} = 0$ appear completely unaffected by the addition of shear, resulting in a nearly identical growth rate of the fastest growing mode of the system. This does show that there are many fewer unstable modes in the sheared case, which could easily contribute to the lowered fluxes in the case with constant shear.

Figure 9 shows the growth rates across wavenumber for two cases with $\gamma_x = \sqrt{5/4}$ one of which has unidirectional oscillating shear and the other of which has rotational shear. The first major result here is that the y–z wavenumber dependence of the oscillating shear case is identical to both the prior cases; that is, because there is no y-directional shear, the $\tilde{k}_{\mathrm{M},x} = 0$ modes are unaffected. Such is not the case for the rotational shear, which does show substantial reduction both in the magnitude of the growth rates and in the range of wavenumbers for which large growth rates are seen. An analogous effect is seen in the $\tilde{k}_{\mathrm{M},x} = 0$ modes in both cases, clearly indicating that the oscillating nature of both shear setups are inhibiting the modes but not eliminating them entirely as in the constant shear case. The maximum growth rate of the unidirectional oscillating shear case remains largely unchanged from the original salt-fingering case, which likely explains why the dependence on ω is relatively weak. If we postulate that the final equilibrium fluxes are determined primarily by the maximum growth rate and secondarily by the number of unstable modes, then it would be expected that the unidirectional os-

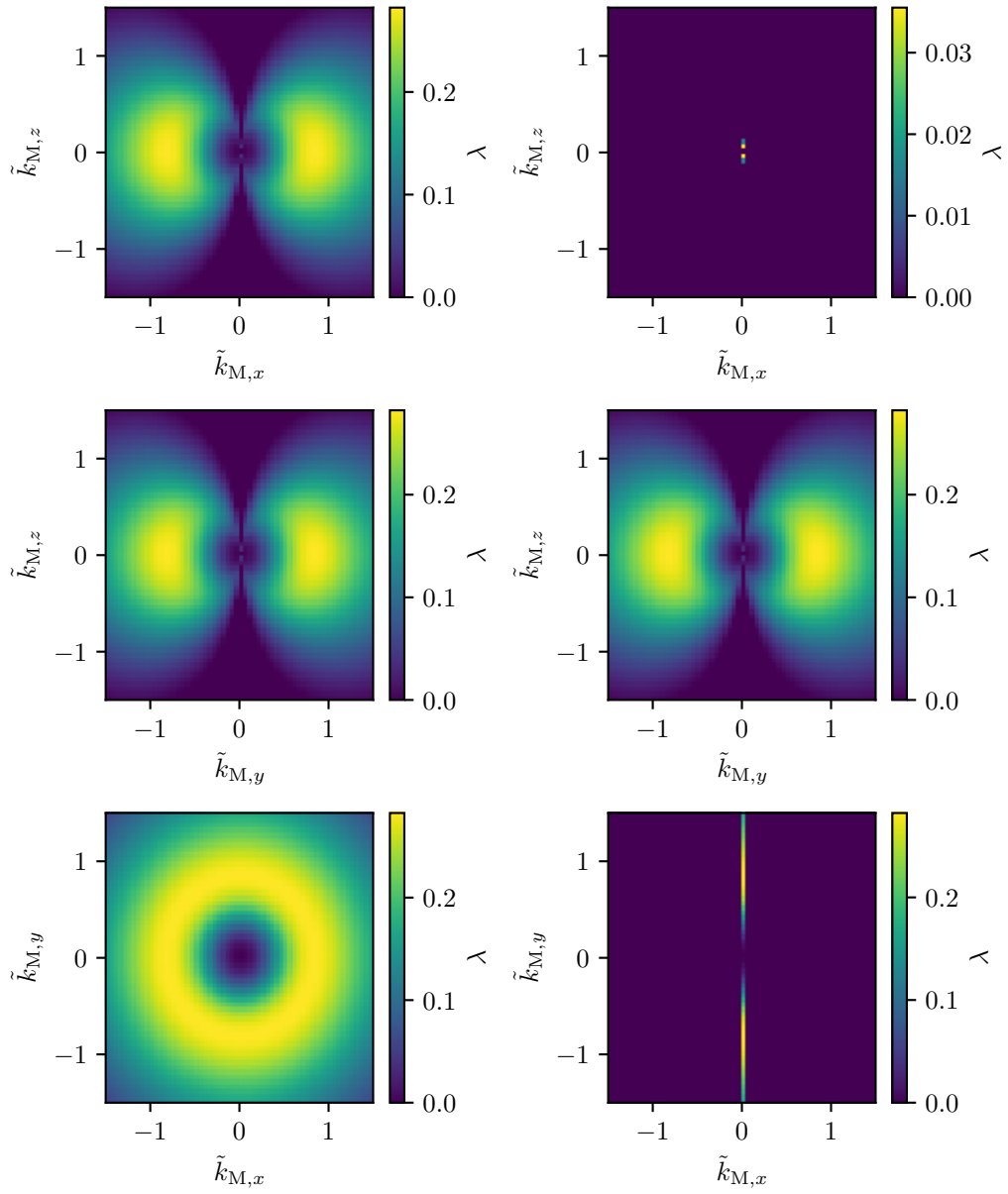

Figure 8. (left) The growth rate of a mode of given wavenumber for the salt-fingering case in the absence of shear. (top) A cross section of wavenumber space at $k_y = 0$. (middle) A cross section of wavenumber space at $k_x = 0$. (bottom) A cross section of wavenumber space at $k_z = 0$. (right) An analogous set of plots for a case with constant shear, $\gamma_x = \sqrt{5/4}$, $\gamma_y = 0$, $\omega = 0$.

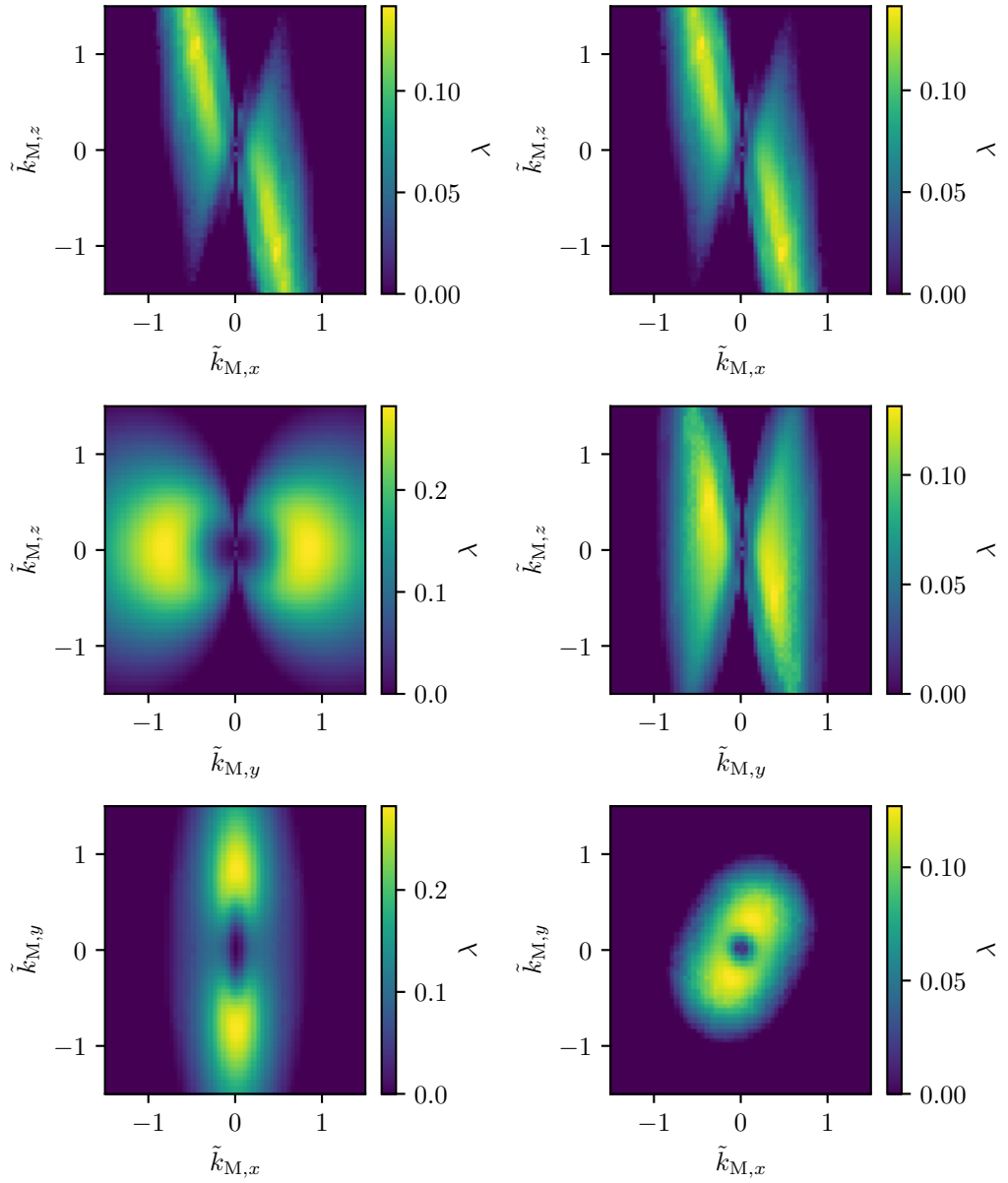

Figure 9. (left) The growth rate of a mode of given wavenumber for the salt-fingering case with oscillating unidirectional shear: $\gamma_x = \sqrt{5/4}$, $\gamma_y = 0$, $\omega = 0.1\pi$ plotted in the same manner as in Figure 8. (right) An analogous set of plots for a case with rotating shear: $\gamma_x = \gamma_y = \sqrt{5/4}$, $\omega = 0.1\pi$.

cillating cases are generally of higher flux than comparable rotational cases, and that there is a weak dependence of flux on ω, as was observed in Figure 7.

We highlight the dependence of the growth rates on ω in Figure 10 by illustrating the same manner of figure as Figure 9 but with $\omega = 0.4\pi$. As in the prior $\omega = 0.1\pi$ case, the rotating setup shows weaker growth rates than the original, pure salt-fingering case, and the vertical structure of the growth rates in wavenumber space bow inward for $\tilde{k}_{\mathrm{M},z} = 0$, resulting in fewer unstable modes which are weaker overall, but this effect is not as extreme as it was for the analogous case with $\omega = 0.1\pi$. Shear has a similar reduced impact on the unidirectional case. As before, the unidirectional case shows no substantial impact from shear for modes with $\tilde{k}_{\mathrm{M},x} = 0$, but the width of the torus in $\tilde{k}_{\mathrm{M},y} = 0$ is substantially larger than for the case with $\omega = 0.1\pi$. The effect of ω follows from the consequence that faster oscillations with the same given maximum shear result in less deformation of the fingering structures and therefore, fewer modes are impacted. We also compare the growth rates of the simplified linear system to the full results in Figure 11 for a range of ω for rotating shear with $\mathrm{Ri} = 2$. These confirm the general result that the growth rates of the system generally increase with ω and that the linear theory reasonably predicts the initial growth of the nonlinear system. The case of $\omega = 0$ is exceptional because in that limit, the shear becomes unidirectional, and the growth rate is comparable to the original salt-fingering shear.

The behavior of the growth rates, while qualitatively similar to the results of Radko and Smith (2012), present a picture perhaps in contrast to their growth-rate balance theory. Growth-rate balance theory postulates that the system achieves its steady-state equilibrium when the primary (in this case the salt-fingering) instability grows at a comparable rate to the secondary (in this case, the zig-zag) instability. This typically means that cases with larger growth rates (but comparable geometry) are more difficult to disrupt by secondary instabilities and therefore have stronger fluxes at the time of equilibrium; however, we have shown many cases where the growth rates are comparable and the fastest growing mode has roughly the same wave vector but where the final fluxes differ by more than a factor of two. This would seem to preclude the use of growth-rate balance theory to quantify this effect.

6 Conclusions

We have characterized through numerical simulations the effects of oscillating shear on ordinary salt fingers. In general, it is found that shear universally inhibits the development of salt fingers as first mentioned by Linden (1974). This results in weaker mixing in all cases, which is consistent with prior work (e.g., Fernandes & Krishnamurti, 2010; Kimura & Smyth, 2007). It is shown that shear inhibits fingering unstable modes with horizontal wave vectors that are parallel to the shear, generating salt sheets. However, when the direction of shear changes with time, this effect can damp all fingering unstable modes.

It is shown that the final thermal and haline fluxes of the simulations are also reduced in all sheared cases. This is attributed to two main factors: the maximum growth rate of the system and the number of modes with large growth rates. In the case of unidirectional shear, the maximum growth rate is unchanged as the modes with wave vectors perpendicular to the shear are not affected, but many of the modes are inhibited, and the fluxes are lowered. In the case with rotational shear, the modes are uniformly inhibited, which results in a lower maximum growth rate and therefore decreased fluxes as well. In addition, the frequency of the shear is also important to determining the final fluxes of the salt fingers, which is due to the capacity of the shear to deform the fingers themselves. For large frequencies (and given maximum shear), the maximum inclination of the fingers is minimal, and the growth rates of the individual modes are minimally affected. The range of internal wave periods considered in this study span from

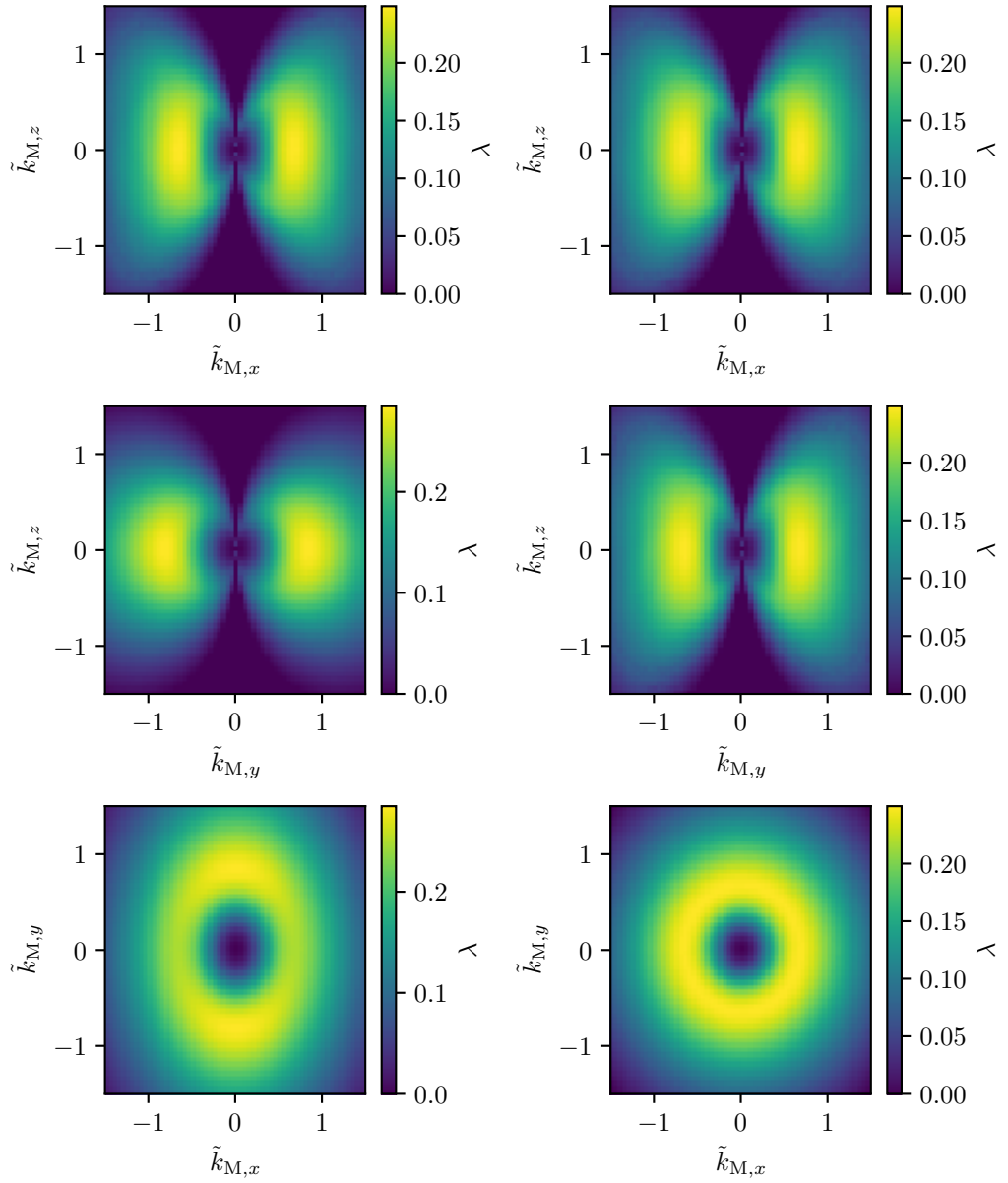

Figure 10. (left) The growth rate of a mode of given wavenumber for the salt-fingering case with oscillating unidirectional shear: $\gamma_x = \sqrt{5/4}$, $\gamma_y = 0$, $\omega = 0.4\pi$ plotted in the same manner as in Figure 8. (right) An analogous set of plots for a case with rotating shear: $\gamma_x = \gamma_y\sqrt{5/4}$, $\omega = 0.4\pi$.

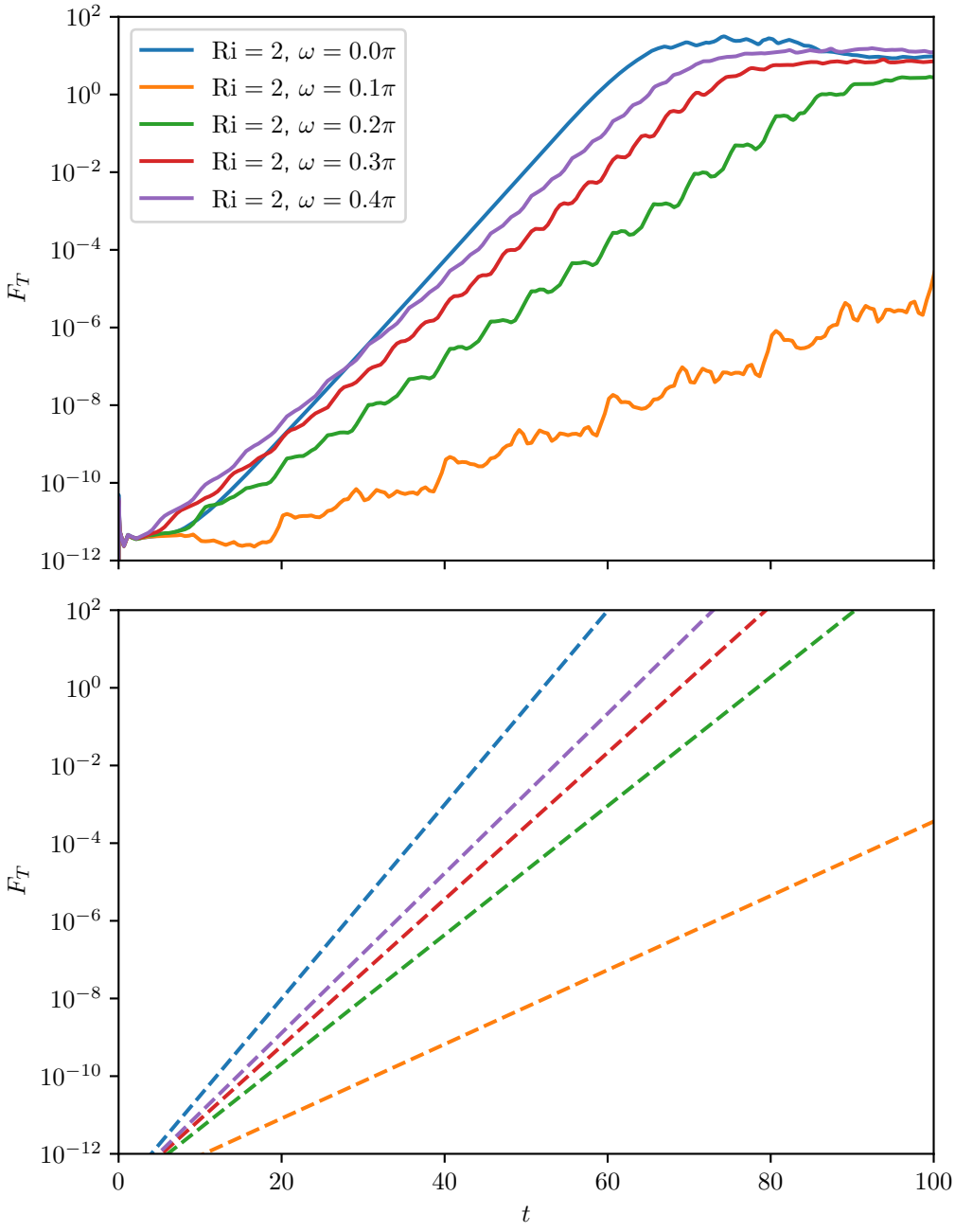

Figure 11. (top) The thermal fluxes from rotating simulations with Ri=2 while they are still in the early phase when exponential growth is apparent. (bottom) Predictions of growth rates from linear theory.

1–4 hours in dimensional units. Many of the strongest internal waves in the ocean are near the inertial frequency and vary slowly in direction, which would suggest that our low-frequency rotating setup is most appropriate for approximating fluxes in the ocean. However, from our simulations at low-frequencies or constant shear, it is clear that near-inertial frequencies could potentially limit the unstable wave modes to low wavenumbers. Resolving such systems with a spectral method requires fine spectral resolution (or equivalently, large domain sizes), which would be computationally prohibitive at present. For cases with $\mathrm{Ri} > 2$, the difference between constant shear and rotating shear at low frequencies appears to be small.

One of the major applications of this work is its potential implications for larger-scale numerical modeling. Many predictive models of ocean behavior require the modeling of small-scale processes such as salt-fingers, which forms a fundamental building block for these models. Such models span from sizes on the order of tens of meters (such as models of intrusions, e.g., Merryfield, 2002; Mueller et al., 2007) to larger-scale models, such as HYCOM (Halliwell, 2004) and MITgcm (Marshall et al., 1997), which can use the KPP model to parameterize the effects of double-diffusion (Large et al., 1994). The KPP model uses a single parameter (the density ratio) to fully characterize the effects of double-diffusion, and only considers the effects of shear for $\mathrm{Ri} < 0.7$. For near-inertial waves at Richardson numbers around 10, the likes of which would be common in such models, this work would predict that thermal and haline fluxes of salt fingers are reduced by a factor of about 2. For stronger shear, this number increases to about 3 for $\mathrm{Ri} = 4$. This would mean that any such global models could currently be substantially overpredicting the mixing caused by salt-fingering in the ocean.

This work promotes several avenues of further research. The code presented here has many generalizations, not just in the field of double-diffusive convection but also in single-component systems in the presence of shear, such as the time-dependent shear instability described in Radko (2019). In addition, a larger body of such simulations of salt fingers in the presence of shear could lead to a reasonable functional form for these fluxes that could then be implemented into larger ocean models for the purpose of more accurate climate predictions. Finally, additional simulations could be performed on the effects that shear has on thermohaline staircases. While the numerical model developed and used here to study double-diffusive phenomena in large-scale shear, it could be readily applied to other forms of fine- and micro-scale processes in the ocean, which include Kelvin-Helmholtz and Holmboe instabilities.

Appendix A Derivation of the Sheared Mode-Equations

To simplify Equations 6–9 in the tilting coordinate system, we construct a Fourier solution in this coordinate system, which follows the fluid displacement by the background flow. The coordinate transformation described in Equations 14–17 results in the following:

$$\frac{\partial}{\partial x} = \frac{\partial}{\partial \tilde{x}} \tag{A1}$$

$$\frac{\partial}{\partial y} = \frac{\partial}{\partial \tilde{y}} \tag{A2}$$

$$\frac{\partial}{\partial z} = \frac{\partial}{\partial \tilde{z}} - \frac{\gamma_x}{\omega}\sin\omega\tilde{t}\frac{\partial}{\partial \tilde{x}} - \frac{\gamma_y}{\omega}\sin\left(\omega\tilde{t}+\phi\right)\frac{\partial}{\partial \tilde{y}} \tag{A3}$$

$$\frac{\partial}{\partial t} = \frac{\partial}{\partial \tilde{t}} - \gamma_x\tilde{z}\cos\omega\tilde{t}\frac{\partial}{\partial \tilde{x}} - \gamma_y\tilde{z}\cos\left(\omega\tilde{t}+\phi\right)\frac{\partial}{\partial \tilde{y}} \tag{A4}$$

$$\nabla = \left(\frac{\partial}{\partial x}, \frac{\partial}{\partial y}, \frac{\partial}{\partial z}\right). \tag{A5}$$

We desire our results to be periodic in this new coordinate system, so we approximate the solution with a finite number of Fourier modes of the form

$$q\left(\mathbf{x},t\right)=\sum_{l=-3N_x/2}^{3N_x/2}\sum_{m=-3N_y/2}^{3N_y/2}\sum_{n=-3N_z/2}^{3N_z/2}q_{l,m,n}\left(t\right)e^{i\tilde{\mathbf{k}}_{l,m,n}\cdot\tilde{\mathbf{x}}}, \tag{A6}$$

where q represents a generic field, $\tilde{\mathbf{x}}\equiv\left(\tilde{x},\tilde{y},\tilde{z}\right)$, and $\tilde{\mathbf{k}}_{l,m,n}\equiv\left(l\tilde{k}_x,m\tilde{k}_y,n\tilde{k}_z\right)$. The desired modes of the solution range from $l=[-N_x,N_x]$, $m=[-N_y,N_y]$, and $n=[-N_z,N_z]$, and the modes outside that range are included solely to account for the aliasing of the non-linear terms in the equations, which will be described later. Because the data are real, the negative l modes are chosen to be the complex conjugates of the corresponding positive l modes and are therefore not stored in memory; similarly, the highest order mode in each dimension (at the Nyquist frequency) contains redundant information between positive and negative indices and so the FFT only calculates one, making the total number of tracked modes $\left(\frac{3N_x}{2}+1\right)\times3N_y\times3N_z$ and the number of active modes (after de-aliasing) $(N_x+1)\times2N_y\times2N_z$. The quantities $\tilde{k}_x$, $\tilde{k}_y$, and $\tilde{k}_z$ are the lowest non-zero wave numbers in the system, which has dimensions Γ_x by Γ_y by Γ_z. It is important to note that the use of vector notation here is purely for notational convenience in representing the exponential argument; all vector math in this study occurs only in the stationary coordinate system because the basis vectors in the tilting coordinate system do not form an orthonormal set. For convenience, we define $k'_{l,m,n}\left(\tilde{t}\right)\equiv n\tilde{k}_z-l\tilde{k}_x\frac{\gamma_x}{\omega}\sin\omega\tilde{t}-m\tilde{k}_y\frac{\gamma_y}{\omega}\sin\left(\omega\tilde{t}+\phi\right)$ and $\mathbf{k}_{l,m,n}\equiv l\tilde{k}_x\mathbf{e}_x+m\tilde{k}_y\mathbf{e}_y+k'_{l,m,n}\mathbf{e}_z$ such that

$$\nabla e^{i\tilde{\mathbf{k}}_{l,m,n}\cdot\tilde{\mathbf{x}}} = \left(il\tilde{k}_x\mathbf{e}_x+im\tilde{k}_y\mathbf{e}_y+ik'_{l,m,n}\mathbf{e}_z\right)e^{i\tilde{\mathbf{k}}_{l,m,n}\cdot\tilde{\mathbf{x}}} \tag{A7}$$

$$= i\mathbf{k}_{l,m,n}e^{i\tilde{\mathbf{k}}_{l,m,n}\cdot\tilde{\mathbf{x}}}. \tag{A8}$$

As the notation suggests, $k'_{l,m,n}$ is the vertical wavenumber in the stationary system and $\mathbf{k}_{l,m,n}$ represents the wave vector in the stationary system, which is a quantity which recurs regularly in the sheared governing equations.

We use Equations A1–A5 to reconstruct the governing equations in our sheared coordinate system. Taking, for example, the temperature equation, we find

$$\left(\frac{\partial}{\partial\tilde{t}}-\gamma_x z\cos\omega\tilde{t}\frac{\partial}{\partial\tilde{x}}-\gamma_y z\cos\left(\omega\tilde{t}+\phi\right)\frac{\partial}{\partial\tilde{y}}\right)T$$

$$+\tilde{\mathbf{u}}\cdot\nabla T+\gamma_x z\cos\omega\tilde{t}\frac{\partial}{\partial\tilde{x}}T+\gamma_y z\cos\left(\omega\tilde{t}+\phi\right)\frac{\partial}{\partial\tilde{y}}T+sw = \nabla^2T \tag{A9}$$

$$\frac{\partial}{\partial\tilde{t}}T+\tilde{\mathbf{u}}\cdot\nabla T+sw = \nabla^2T. \tag{A10}$$

It is important to note that the gradient and Laplacian operators are still in the original vertical coordinate system. We isolate the l,m,n mode of the system by recognizing that the Fourier modes are orthogonal:

$$\frac{\partial}{\partial\tilde{t}}T_{l,m,n}+\left(\tilde{\mathbf{u}}\cdot\nabla T\right)_{l,m,n}+sw_{l,m,n} = -\mathbf{k}^2_{l,m,n}T_{l,m,n}, \tag{A11}$$

where we have denoted the l,m,n mode of the nonlinear term as

$$\left(\tilde{\mathbf{u}}\cdot\nabla T\right)_{l,m,n}\equiv\frac{1}{\Gamma_x\Gamma_y\Gamma_z}\int_0^{\Gamma_x}\int_0^{\Gamma_y}\int_0^{\Gamma_z}\left(\tilde{\mathbf{u}}\cdot\nabla T\right)e^{-i\tilde{\mathbf{k}}_{l,m,n}\cdot\tilde{\mathbf{x}}}d\tilde{x}d\tilde{y}d\tilde{z}. \tag{A12}$$

Using the same method for the remaining equations results in the following:

$$\frac{1}{\mathrm{Pr}}\left(\frac{\partial}{\partial\tilde{t}}\tilde{u}_{l,m,n}+\left(\tilde{\mathbf{u}}\cdot\nabla\tilde{u}\right)_{l,m,n}+w_{l,m,n}\frac{\partial\overline{u}}{\partial z}\right) = -il\tilde{k}_x p_{l,m,n}-\mathbf{k}^2_{l,m,n}\tilde{u}_{l,m,n}, \quad \text{(A13)}$$

$$\frac{1}{\mathrm{Pr}}\left(\frac{\partial}{\partial\tilde{t}}\tilde{v}_{l,m,n}+\left(\tilde{\mathbf{u}}\cdot\nabla\tilde{v}\right)_{l,m,n}+w_{l,m,n}\frac{\partial\overline{v}}{\partial z}\right) = -im\tilde{k}_y p_{l,m,n}-\mathbf{k}^2_{l,m,n}\tilde{v}_{l,m,n}, \quad \text{(A14)}$$

$$\frac{1}{\mathrm{Pr}}\left(\frac{\partial}{\partial\tilde{t}}w_{l,m,n}+\left(\tilde{\mathbf{u}}\cdot\nabla w\right)_{l,m,n}\right) = -ik'_{l,m,n}p_{l,m,n}-\mathbf{k}^2_{l,m,n}w_{l,m,n}$$

$$+T_{l,m,n}-S_{l,m,n}, \quad \text{(A15)}$$

$$\frac{\partial}{\partial\tilde{t}}T_{l,m,n}+\left(\tilde{\mathbf{u}}\cdot\nabla T\right)_{l,m,n}+sw_{l,m,n} = -\mathbf{k}^2_{l,m,n}T_{l,m,n}, \quad \text{(A16)}$$

$$\frac{\partial}{\partial\tilde{t}}S_{l,m,n}+\left(\tilde{\mathbf{u}}\cdot\nabla S\right)_{l,m,n}+sR_0^{-1}w_{l,m,n} = -\tau\mathbf{k}^2_{l,m,n}S_{l,m,n}, \quad \text{(A17)}$$

$$l\tilde{k}_x\tilde{u}_{l,m,n}+m\tilde{k}_y\tilde{v}_{l,m,n}+k'_{l,m,n}w_{l,m,n} = 0. \quad \text{(A18)}$$

Because of the orthogonality of the Fourier modes in the decomposition, the linear terms are trivial to evaluate; however, the nonlinear terms require more attention. Each nonlinear term is of the form $\tilde{\mathbf{u}}\cdot\nabla q$. To maintain spectral accuracy of the calculation, the gradients in these terms should be evaluated in spectral space, which is equivalent to multiplying the field by $i\mathbf{k}_{l,m,n}$, so

$$\nabla q=\sum_{l=-N_x}^{N_x}\sum_{m=-N_y}^{N_y}\sum_{n=-N_z}^{N_z}i\mathbf{k}_{l,m,n}q_{l,m,n}e^{i\tilde{\mathbf{k}}_{l,m,n}\cdot\tilde{\mathbf{x}}}, \quad \text{(A19)}$$

for a generic field q. The product of $\tilde{\mathbf{u}}$ and ∇q is considerably more computationally expensive in spectral space and would require the use of, for example, a Gallerkin method. In order to instead evaluate the product in physical space, this will require several Fourier transforms to convert the field and derivative to physical space, where the multiplication is performed, before transforming the result back to spectral space.

Appendix B Patterson–Orszag Adaptation in Sheared Coordinates

The time-stepping algorithm used in the code is a combined third-order Adams–Bashforth scheme for the explicit terms with a third-order Backwards Differentiation Formula for the implicit terms. For the buoyancy equations (even in the sheared reference frame), these are straightforward to implement and so are not described in detail here. However, for the momentum equation, we also use an adapted Patterson–Orszag algorithm to ensure that the fluid remains incompressible, which requires moderate adaptation for this problem. Traditionally, this algorithm calculates the pressure required to ensure the fluid remains incompressible, but this has some complications for a moving coordinate system which should become apparent. We begin with the general equation of the integration of velocity from time $\tilde{t}_{r-1}$ to $\tilde{t}_r$:

$$\sum_{j=0}^{3}a_j\tilde{\mathbf{u}}_{l,m,n}\left(\tilde{t}_{r-j}\right) = \Delta\tilde{t}\sum_{j=1}^{3}b_j\mathbf{f}_{l,m,n}\left(\tilde{t}_{r-j},\tilde{\mathbf{u}}\left(\tilde{t}_{r-j}\right),T\left(\tilde{t}_{r-j}\right),S\left(\tilde{t}_{r-j}\right)\right)$$

$$+\Delta\tilde{t}\mathbf{g}_{l,m,n}\left(\tilde{t}_r,\tilde{\mathbf{u}}\left(\tilde{t}_r\right),T\left(\tilde{t}_r\right),S\left(\tilde{t}_r\right)\right)$$

$$-\Delta\tilde{t}\sum_{j=1}^{3}b_j i\mathbf{k}_{l,m,n}\left(\tilde{t}_r\right)p_{l,m,n}\left(\tilde{t}_{r-1}\right), \quad \text{(B1)}$$

where we have separated the time derivatives of a single mode into components

$$\frac{\partial}{\partial\tilde{t}}\tilde{\mathbf{u}}_{l,m,n}\left(\tilde{t}\right) = \mathbf{f}_{l,m,n}\left(\tilde{t},\tilde{\mathbf{u}}\left(\tilde{t}\right),T\left(\tilde{t}\right),S\left(\tilde{t}\right)\right)$$

$$+\mathbf{g}_{l,m,n}\left(\tilde{t},\tilde{\mathbf{u}}\left(\tilde{t}\right),T\left(\tilde{t}\right),S\left(\tilde{t}\right)\right)-i\mathbf{k}_{l,m,n}\left(\tilde{t}\right)p_{l,m,n}, \quad \text{(B2)}$$

where $\mathbf{g}_{l,m,n}$ denotes the operators treated implicitly (diffusive processes) and $\mathbf{f}_{l,m,n}$ denotes the operators treated explicitly (buoyancy, advection). This scheme is third-order accurate in time.

The pressure term is included separately from the explicit terms for reasons that will become clear. This algorithm is not a predictor–corrector method and in fact, $\mathbf{f}$ and $\mathbf{g}$ are always evaluated such that the temporal argument of the derivative is the same as that of the dependent variables. As such, we adopt the shorthand that $\mathbf{f}_{l,m,n}\left(\tilde{t}\right) = \mathbf{f}_{l,m,n}\left(\tilde{t}, \tilde{\mathbf{u}}\left(\tilde{t}\right), T\left(\tilde{t}\right), S\left(\tilde{t}\right)\right)$. It is worth noting that the coefficients a and b can be determined by the method of undetermined coefficients by ensuring first that a system with $\mathbf{f} = 0$ is accurate to third order (to determine a) and then by ensuring that a system with $\mathbf{g} = 0$ is accurate to the same order (to determine b). Since the timestep in this code is adaptive, these numbers must be recalculated each timestep, but the math is simple, if tedious.

To enforce that the next step is divergence-free, we must calculate the requisite pressure to ensure that the divergence of the velocity at $\tilde{t} = \tilde{t}_r$, which we denote using $\nabla_r \equiv \left(\frac{\partial}{\partial \tilde{x}}, \frac{\partial}{\partial \tilde{z}} - \frac{\gamma_x}{\omega}\sin\omega\tilde{t}_r \frac{\partial}{\partial \tilde{x}} - \frac{\gamma_y}{\omega}\sin\left(\omega\tilde{t}_r + \phi\right)\frac{\partial}{\partial \tilde{y}}\right)$. If we take Equation B1 and require that $\nabla_r \cdot \tilde{\mathbf{u}}_{l,m}\left(\tilde{t}_r\right) e^{i\tilde{\mathbf{k}}_{l,m,n}\cdot\tilde{\mathbf{x}}} = 0$, we can solve for the pressure:

$$\sum_{j=1}^{3} a_j \nabla_r \cdot \tilde{\mathbf{u}}_{l,m,n}\left(\tilde{t}_{r-j}\right) e^{i\tilde{\mathbf{k}}_{l,m,n}\cdot\tilde{\mathbf{x}}} = \Delta\tilde{t}\sum_{j=1}^{3} b_j \nabla_r \cdot \mathbf{f}_{l,m,n}\left(\tilde{t}_{r-j}\right) e^{i\tilde{\mathbf{k}}_{l,m,n}\cdot\tilde{\mathbf{x}}} \tag{B3}$$

$$+\Delta\tilde{t}\nabla_r \cdot \mathbf{g}_{l,m,n}\left(\tilde{t}_r\right) e^{i\tilde{\mathbf{k}}_{l,m,n}\cdot\tilde{\mathbf{x}}} \tag{B4}$$

$$-\nabla_r \cdot \Delta\tilde{t}\sum_{j=1}^{3} b_j i\mathbf{k}_{l,m,n}\left(\tilde{t}_r\right) p_{l,m,n}\left(\tilde{t}_{r-j}\right) e^{i\tilde{\mathbf{k}}_{l,m,n}\cdot\tilde{\mathbf{x}}}.$$

Because $\mathbf{g}_{l,m,n}\left(\tilde{t}_r\right) = -\mathrm{Pr}\left(l^2k_x^2 + m^2k_y^2 + {k'}^2_{l,m,n}\left(\tilde{t}_r\right)\right)\tilde{\mathbf{u}}_{l,m,n}\left(\tilde{t}_r\right)$, our requirement that $\nabla_r \cdot \tilde{\mathbf{u}}_{l,m}\left(\tilde{t}_r\right) e^{i\tilde{\mathbf{k}}_{l,m,n}\cdot\tilde{\mathbf{x}}} = 0$ means that the divergence of $\mathbf{g}_{l,m,n}\left(\tilde{t}_r\right) e^{i\tilde{\mathbf{k}}_{l,m,n}\cdot\tilde{\mathbf{x}}}$ is also guaranteed to be zero. Thus, Equation B5 can be rewritten as

$$\sum_{j=1}^{3} a_j i\mathbf{k}_{l,m,n}\left(\tilde{t}_r\right) \cdot \tilde{\mathbf{u}}_{l,m,n}\left(\tilde{t}_{r-j}\right) = \Delta\tilde{t}\sum_{j=1}^{3} b_j i\mathbf{k}_{l,m,n}\left(\tilde{t}_r\right) \cdot \mathbf{f}_{l,m,n}\left(\tilde{t}_{r-j}\right) \tag{B5}$$

$$+\Delta\tilde{t}\sum_{j=1}^{3} b_j \mathbf{k}_{l,m,n}\left(\tilde{t}_r\right) \cdot \mathbf{k}_{l,m,n}\left(\tilde{t}_{r-j}\right) p_{l,m,n}\left(\tilde{t}_{r-j}\right) \tag{B6}$$

Given that the pressure, velocity, and $\mathbf{f}$ have all been calculated for the previous timesteps, and the velocity and $\mathbf{f}$ are known for the current timestep, it is possible to solve this equation for $p_{l,m,n}\left(\tilde{t}_{r-1}\right)$.

Acknowledgments

The authors would like to thank Stephan Stellmach for writing the first version of the Traxler et al. (2011) code upon which this study was built. Support of the National Science Foundation (grant OCE 1756491) is gratefully acknowledged. The first author was supported through the National Research Council Research Associateship Program for part of this research. The authors acknowledge the Texas Advanced Computing Center (TACC) at The University of Texas at Austin for providing HPC resources that have contributed to the research results reported within this paper. URL: http://www.tacc.utexas.edu

Datasets produced in this study are available in Brown, Justin (2021), "Salt Fingers in the Presence of Uniform Shear: Data from Numerical Simulations", Mendeley Data, V1, doi: 10.17632/mwpvysxyvp.1

References

Baines, P. G. G., & Gill, A. E. (1969). On thermohaline convection with linear gradients. *Journal of Fluid Mechanics*, *37*(02), 289 306. doi: 10.1017/s0022112069000553

Canuto, C., Quarteroni, A., Hussaini, M. Y., & Zang, T. A. (2007). *Spectral Methods*. (Spectral Model for Incompressibility in Sheared Environments SMISE) doi: 10.1007/978-3-540-30728-0

Delorme, P. (1985). Simulation numerique de turbulence homogene compressible avec ou sans cisaillement impose. *these de docteur ingenieur, Universite de Poitiers*.

Fernandes, A. M., & Krishnamurti, R. (2010). Salt finger fluxes in a laminar shear flow. *Journal of Fluid Mechanics*, *658*, 148 165. doi: 10.1017/s0022112010001588

Frigo, M. (1999). A fast Fourier transform compiler. *ACM SIGPLAN Notices*, *34*(5), 169–180. doi: 10.1145/301618.301661

Halliwell, G. R. (2004). Evaluation of vertical coordinate and vertical mixing algorithms in the HYbrid-Coordinate Ocean Model (HYCOM). *Ocean Modelling*, *7*(3-4), 285–322. doi: 10.1016/j.ocemod.2003.10.002

Kimura, S., & Smyth, W. (2007). Direct numerical simulation of salt sheets and turbulence in a double-diffusive shear layer. *Geophysical Research Letters*, *34*(21), L21610. doi: 10.1029/2007gl031935

Kimura, S., & Smyth, W. (2011, 01). Secondary instability of salt sheets. *Journal of Marine Research*, *69*(1), 57–77. doi: 10.1357/002224011798147624

Kunze, E. (1990, 08). The evolution of salt fingers in inertial wave shear. *Journal of Marine Research*, *48*(3), 471 504. doi: 10.1357/002224090784984696

Kunze, E., Williams, A. J., & Schmitt, R. W. (1987). Optical microstructure in the thermohaline staircase east of Barbados. *Deep Sea Research Part A*, *34*(1), 1697 1704. doi: 10.1016/0198-0149(87)90018-5

Large, W. G., McWilliams, J. C., & Doney, S. C. (1994). Oceanic vertical mixing: A review and a model with a nonlocal boundary layer parameterization. *Reviews of Geophysics*, *32*(4), 363 403. doi: 10.1029/94rg01872

Linden, P. F. (1971). Salt fingers in the presence of grid-generated turbulence. *Journal of Fluid Mechanics*, *49*(3), 611–624. doi: 10.1017/s0022112071002283

Linden, P. F. (1974, 10). Salt fingers in a steady shear flow. *Geophysical & Astrophysical Fluid Dynamics*, *6*(1), 1 27. doi: 10.1080/03091927409365785

Marshall, J., Adcroft, A., Hill, C., Perelman, L., & Heisey, C. (1997). A finite-volume, incompressible Navier Stokes model for studies of the ocean on parallel computers. *Journal of Geophysical Research Oceans*, *102*(C3), 5753 5766. (Describes the numerical scheme of MITgcm) doi: 10.1029/96jc02775

Merryfield, W. J. (2002). Intrusions in Double-Diffusively Stable Arctic Waters: Evidence for Differential Mixing? *Journal of Physical Oceanography*, *32*(5), 1452–1459. doi: 10.1175/1520-0485(2002)032⟨1452:iiddsa⟩2.0.co;2

Mueller, R. D., Smyth, W. D., & Ruddick, B. (2007). Shear and Convective Turbulence in a Model of Thermohaline Intrusions. *Journal of Physical Oceanography*, *37*(10), 2534–2549. doi: 10.1175/jpo3137.1

Radko, T. (2013). Double-Diffusive Convection. *Double-Diffusive Convection*. doi: 10.1017/cbo9781139034173.016

Radko, T. (2019, 01). Thermohaline-Shear Instability. *Geophysical Research Letters*, *46*(2), 822 832. doi: 10.1029/2018gl081009

Radko, T., Ball, J., Colosi, J., & Flanagan, J. D. (2015). Double-Diffusive Convection in a Stochastic Shear. *Journal of Physical Oceanography*, *45*(12), 3155 3167. doi: 10.1175/jpo-d-15-0051.1

Radko, T., & Smith, D. P. (2012). Equilibrium transport in double-diffusive convection. *Journal of Fluid Mechanics*, *692*, 5 27. doi: 10.1017/jfm.2011.343

Rogallo, R. S. (1981). *Numerical Experiments in Homogeneous Turbulence* (Tech. Rep.). Retrieved from `https://ntrs.nasa.gov/citations/19810022965`

Stellmach, S., & Hansen, U. (2008). An efficient spectral method for the simulation of dynamos in Cartesian geometry and its implementation on massively parallel computers. *Geochemistry, Geophysics, Geosystems*, *9*(5), 1–11. doi: 10.1029/2007gc001778

Stern, M. E. (1960). The "Salt-Fountain" and Thermohaline Convection. *Tellus A*, *12*(2), 172 175. doi: 10.1111/j.2153-3490.1960.tb01295.x

Stommel, H., Arons, A. B., & Blanchard, D. (1956). An oceanographical curiosity: the perpetual salt fountain. *Deep Sea Research*, *3*(2), 152 153. doi: 10.1016/0146-6313(56)90095-8

Traxler, A. L., Stellmach, S., Garaud, P., Radko, T., & Brummell, N. H. (2011). Dynamics of fingering convection. Part 1 Small-scale fluxes and large-scale instabilities. *Journal of Fluid Mechanics*, *677*, 530 553. doi: 10.1017/jfm.2011.98

Zhang, J., Schmitt, R. W., & Huang, R. X. (1998). Sensitivity of the GFDL Modular Ocean Model to Parameterization of Double-Diffusive Processes*. *Journal of Physical Oceanography*, *28*(4), 589–605. doi: 10.1175/1520-0485(1998)028⟨0589:sotgmo⟩2.0.co;2